

MULTIPLE MODE MICROMECHANICAL RESONATORS

Reid A. Brennen, Albert P. Pisano, and William C. Tang

Berkeley Sensor & Actuator Center
Electronics Research Laboratory
Department of Electrical Engineering and Computer Science
University of California, Berkeley CA 94720

ABSTRACT

In this paper are described two resonant micromechanical structures that have been designed, fabricated, and tested and which exhibited multiple modes of vibration. The first had a cantilevered inertial mass that was actuated by a curved-comb electrostatic-drive attached near the root of the cantilever. The second structure had a straight-comb electrostatic-drive with a folded flexure suspension that was used to actuate the cantilevered inertial mass. The first structure exhibited 2 distinct vibration modes, and the second structure actually exhibited 3 distinct vibration modes. An analytic dynamic model has been developed and it predicted the vibrational mode shapes of the structures. Tests of the fabricated structures have demonstrated that peak-to-peak lateral displacements greater than 10 microns were feasible. Further, peak-to-peak angular displacements greater than 10° have been measured during second mode vibration. The resonant frequencies of the structures varied from 1.7 to 33 kHz depending on structure geometry. Cantilever structures with overhang lengths as great as 864 microns have been fabricated and operated with no perceptible contact between the inertial mass and the substrate.

INTRODUCTION

Micro electromechanical resonant systems hold out the promise of providing extremely fine position control at very high mechanical frequencies with extremely low power input. Some microresonators have been shown capable of achieving high frequency resonance (750 kHz) at high Q (above 35,000), when fabricated of polycrystalline silicon and operated in a vacuum [1]. Other microresonators have been designed for relatively large linear motion of a rigid body vibration mode (as opposed to a continuum vibration mode) and these, too, have been shown to achieve significant values of Q (49,000) for large amplitude motion (20 micrometers) at 31 kHz as reported by [2], [3] as well as by [4].

The common feature of all these microresonators is that their vibration mode is purely linear. This is an artifact of the mechanical design features of the flexural suspension systems and the mechanics of the boundary conditions where the flexures are anchored to the substrate. Clearly the designers have explicitly chosen mechanical designs that deliberately preclude rotational motion. Other designs have been tailored to flexural suspensions suitable for purely angular resonance, and such a device is described in [2].

In this research effort, a microresonator has been designed with a flexural suspension that admits resonances in all of translational, rotational, and coupled translational/rotational modes of vibration. These modes are not only well-separated in frequency, but can be selectively excited and analytically predicted. This makes it possible to design a new class of resonant structure micromotors with selectable modes of operation.

Micromotors that attempt to achieve rotational motion without the use of flexures must implement some sort of mechanical bearing in which surface-to-surface contact friction is inevitable [5], [6]. Such micromotors have the advantage of limitless rotation, but this is obtained at the cost of friction and wear. Rotational resonant-structure micromotors may not provide full rotation motion, but operate at high frequency with substantial Q in the complete absence of mechanical friction and wear. Until research in the complete and controlled levitation of armatures in micromechanical rotation motors provides a workable engineering design [7], rotational resonant-structure micromotors seem to offer the only solution to high-frequency, zero wear rotational motion.

In this research, two mechanical designs for multiple-mode, micromechanical resonators have been developed, fabricated, operated, and quantified experimentally. Analytic, dynamic modes have been developed for each, and it is seen that these models predict vibration mode shapes and vibration frequencies.

DESIGN

The two basic designs of the multiple mode resonating structures are shown in Figs. 1 and 2. Both designs are modular two component systems that consist of a "semaphore" and a "driving base". The semaphore section in both designs is the resonator proper, and is made up of a single cantilever beam with an end mass. The beam can be attached at one edge of the plate mass, or, as shown in Figs. 1 and 2, the beam can be attached at the gravity center of the mass. The other end of the semaphore beam is attached to the drive-base, of which two distinct designs are presented below. The drive-base in each case consists of an electrostatic comb drive [3] which is supported by a flexure suspension. The electrostatic drive used two comb elements, one which was used for driving the structure and one which was used to sense frequency.

A cantilever design, as opposed to some variation of a resonant bridge form [3], was used for the semaphore for several reasons. A cantilever beam has 64 times the compliance of an equal length beam that is fixed at the ends, and thus, the cantilever design affords greater compliance in a shorter distance. Further, the cantilever design is a completely released structure that does not retain any residual stresses induced by the fabrication process. Lastly, this design allows an additional degree of freedom in the semaphore mass, a rotational vibration, which can be exploited.

The first of the two designs for the drive-base (Fig. 1) is a linear drive design that uses a folded beam suspension [3] support.

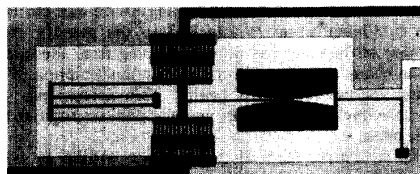


Fig. 1. Photograph of the linear drive multimode resonator structure. Note L-shaped breakaway support attached to the mass to the right.

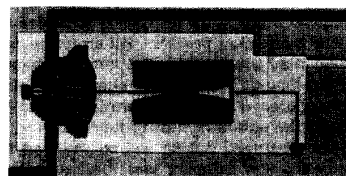


Fig. 2. Photograph of the angular drive multimode resonator structure.

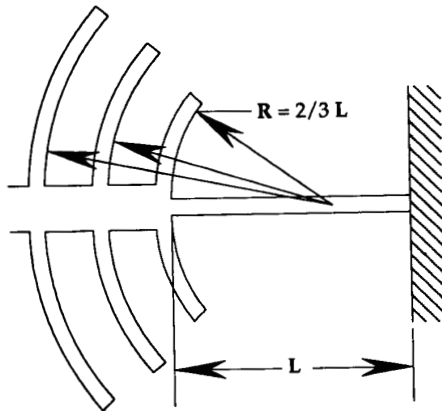


Fig. 3. The center of curvature of the curved comb teeth is set at $1/3$ the distance from the beam root to the comb mass.

This design forces the drive-base to undergo translational motion only, and the semaphore is therefore driven at its beam root only by a translational motion. In contrast, the design shown in Fig. 2 is an angular drive design that employs a drive-base with coupled translational and rotational motion. One way of regarding this second design is to consider it a staged pair of cantilever beams, one each for the drive-base and the semaphore. The complexity of the motion of the drive-base forces the use of curved comb teeth with varying radius of curvature, since displacements are large enough that kinematic nonlinearities must be accounted for. Empirical calculations were used to determine that to provide the maximum clearance between the drive-base comb teeth and the fixed teeth as the drive moves, the center of curvature of the comb teeth must be set to $2/3$ the distance from the beam/comb-structure junction to the supporting beam root, as shown in Fig. 3. Attaching the comb teeth directly to the beam, without local stiffening of the beam at the root of the comb would allow a larger deflection but the resulting design would not allow the use of the empirical tooth curvature result stated above at high resonant frequencies. This design would be undesirable since there would be contact between the fixed- and moving-comb teeth, effectively shorting out the electrostatic comb drive.

The two component system allows a mechanical "impedance matching" in that the high-amplitude semaphore motion can be driven either by large or small base motions. By tuning the physical dimensions and masses of the device components and selecting which resonant mode to excite, the maximum response of the semaphore can be achieved with either large or small base amplitude motion. Since the semaphore cantilever beam is attached to the gravity center, the angular motion of the mass has been decoupled from the translational motion of the beam, and likewise, the translational motion of the mass from the angular motion of the beam. This decoupling makes it possible to selectively excite either translational or angular vibration modes of the mass.

In all structures fabricated, the beam widths as well as the beam thicknesses were nominally $2 \mu\text{m}$. The semaphore mass was 116 by $196 \mu\text{m}$. Each tooth of the electrostatic comb drive was 2 by $2 \mu\text{m}$ in cross section and was separated laterally from the fixed-comb teeth by $2 \mu\text{m}$, as shown in Figs. 4 and 5.

Due to the large size of some of the resonant structures, the total span of the cantilevered section reaches as much as $864 \mu\text{m}$ and a temporary restraint was necessary to prevent structure deflection and damage during the fabrication process. All structures are suspended above the substrate at a $2 \mu\text{m}$ height. Temporary breakaway supports, which can be seen in Figures 1 and 2, were attached to the outside of the mass of the semaphore. These breakaway supports were used to provide strength to the structure during fabrication so that the long structures were not destroyed during wet etching and rinsing. After fabrication, the breakaway support was mechanically removed by physically rupturing it with two probes.

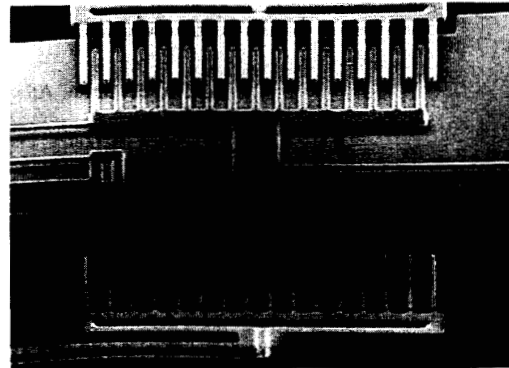


Fig. 4. SEM micrograph of the electrostatic comb drive portion of the linear drive structure.

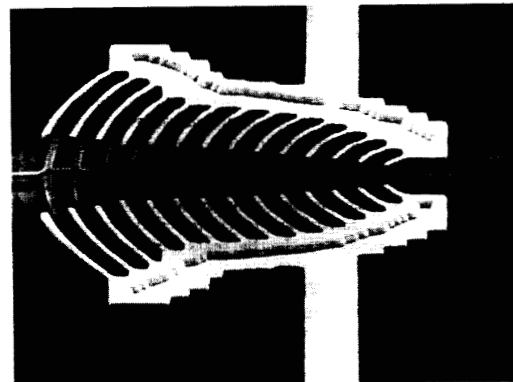


Fig. 5. SEM micrograph of the electrostatic comb drive portion of the angular drive structure.

DYNAMIC MODELLING

Two separate dynamic models were developed to simulate the behavior of the two types of resonant, multimode structures, since each of the drive-bases were fundamentally different for the two designs. The linear-motion drive-base structure with the folded flexure suspension (Fig. 6) had 4 degrees of freedom; 3 translational and 1 rotational. The base drive of this design had 2 degrees of freedom, one being the comb structure mass, the other being the "fold" piece in the folded flexure. As noted above, the semaphore section itself had 2 degrees of freedom, one translational and one rotational, both of which were measured from the equilibrium position of the center of mass of the plate mass. The second structure with the angular drive-base (Fig. 7) also had 4 degrees of freedom, but these were divided into 2 translational and 2 rotational categories. The semaphore for this design was identical to the semaphore used in the linear drive-base design described above, but the driver had 1 translational and 1 rotational degree of freedom.

For the purpose of analyzing the two designs and predicting mode shapes and vibration frequencies, it was assumed that the displacements were small compared to the beam lengths. This assumption would cause some inaccuracies since the experiment did exhibit large amplitude motion, but this inaccuracy turned out to be small. The mass of the beams was ignored in the dynamic model as were any geometric non-linearities such as non-vertical beam sidewalls. In models of both resonators, the flexures were assumed to bend in quasi-static modes; the dynamic deflection shapes of the beam were assumed to closely correspond to the static ones. Although this assumption would be expected to break down at very high frequencies,

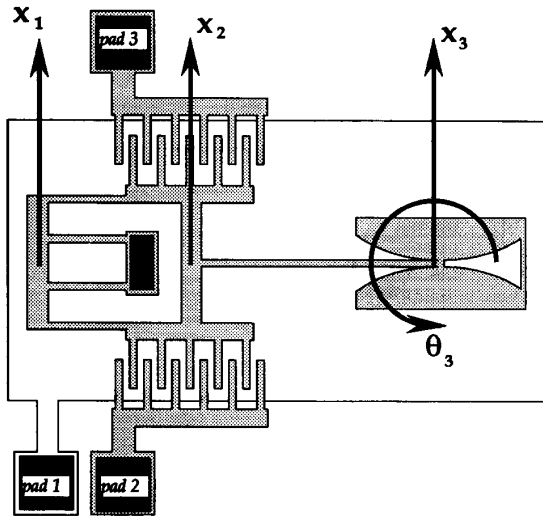


Fig. 6. Schematic drawing of a linear drive multimode resonating structure. The arrows define the degrees of freedom for the structure.

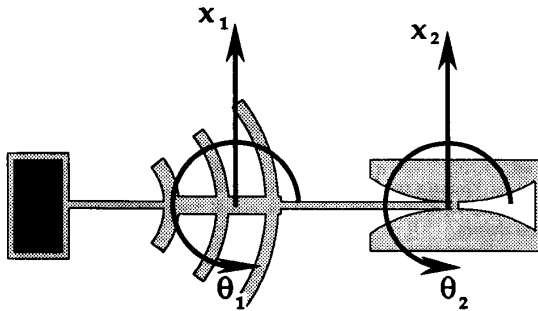


Fig. 7. Schematic drawing of an angular drive multimode resonating structure. The arrows define the degrees of freedom for the structure.

the experimental results indicated that the primary vibration frequencies were not high enough for this assumption to fail.

In these dynamic models, only viscous damping under the masses was considered, even though this was known to result in an underestimate of the actual amount of air damping present at ambient atmospheric pressures [3]. The flow of the air under the semaphore mass was also assumed to be fully developed (i.e. possess a linear velocity profile), and the damping due to drag on the top of the plate (facing away from the substrate) was assumed to be small in this simulation, as was the drag due to the air flow past the edges of the plates and beams. The internal damping in these structures was very small compared to that due to the air and for the purposes of predicting mode shapes and vibration frequencies was likewise assumed to be zero. Since the structure had a constant thickness, and damping was proportional to the area under the mass, the damping acting on the translational mode of vibration was proportional to the mass of each component and the damping of the rotational mode was proportional to the polar moment of inertia of each component. This proportionality between mass and damping comes from the basic assumption of developed flow and the absence of centrifugal motion of the air between the resonating mass and substrate.

Taking a Newtonian approach to dynamics, the inertial forces and moments were set equal and opposite to the summations of forces and moments on each of the masses in the devices. The linear-drive structure had the following coupled equations of motion.

$$\begin{bmatrix} m_1 & 0 & 0 & 0 \\ 0 & m_2 & 0 & 0 \\ 0 & 0 & m_3 & 0 \\ 0 & 0 & 0 & I_{m3} \end{bmatrix} \ddot{\mathbf{v}} + \begin{bmatrix} c_1 & 0 & 0 & 0 \\ 0 & c_2 & 0 & 0 \\ 0 & 0 & c_3 & 0 \\ 0 & 0 & 0 & c_{3\theta} \end{bmatrix} \dot{\mathbf{v}} + \begin{bmatrix} \mathbf{K}_1 \end{bmatrix} \mathbf{v} = 0 \quad (1)$$

where

$$c_i = \frac{\mu}{h} A_i \quad (2) \quad \mathbf{v} = \begin{bmatrix} x_1 \\ x_2 \\ x_3 \\ \theta_3 \end{bmatrix} \quad (4)$$

$$c_{3\theta} = \frac{\mu}{h} J_3 \quad (3)$$

and m_i is the mass of the i^{th} mass, I_{m3} is the mass moment of inertia of the semaphore mass, J_3 is the area moment of inertia of the semaphore mass, h is the gap distance between the semaphore mass and the substrate, μ is the viscosity of air, A_i is the horizontal area of the i^{th} mass, and $[\mathbf{K}_1]$ is the stiffness matrix for the linear drive structure. x_1 , x_2 , x_3 , and θ_3 are defined in Fig. 6. $[\mathbf{K}_1]$ is defined in the Appendix.

The motion of the angular-drive structure was described by a different set of equations of motion:

$$\begin{bmatrix} m_1 & 0 & 0 & 0 \\ 0 & I_{m1} & 0 & 0 \\ 0 & 0 & m_2 & 0 \\ 0 & 0 & 0 & I_{m2} \end{bmatrix} \ddot{\mathbf{U}} + \begin{bmatrix} c_1 & 0 & 0 & 0 \\ 0 & c_{1\theta} & 0 & 0 \\ 0 & 0 & c_2 & 0 \\ 0 & 0 & 0 & c_{2\theta} \end{bmatrix} \dot{\mathbf{U}} + \begin{bmatrix} \mathbf{K}_a \end{bmatrix} \mathbf{U} = 0 \quad (5)$$

where

$$c_i = \frac{\mu}{h} A_i \quad (6) \quad \mathbf{U} = \begin{bmatrix} x_1 \\ \theta_1 \\ x_2 \\ \theta_2 \end{bmatrix} \quad (8)$$

$$c_{j\theta} = \frac{\mu}{h} J_j \quad (7)$$

and m_i is the mass of the i^{th} mass, J_j is the polar moment of inertia of the j^{th} mass, A_i is the horizontal area of the i^{th} mass, and $[\mathbf{K}_a]$ is the stiffness matrix for the angular drive structure. x_1 , θ_1 , x_2 , and θ_2 are defined in Fig. 7. $[\mathbf{K}_a]$ is defined in the Appendix.

By assuming harmonic response to the free vibration problem, each of the above 2 statically coupled sets of matrix equations can be reduced to an eigen problem and solved for their natural (resonant) frequencies and their mode shapes.

It should be noted that in equations (1) and (5) that the stiffness matrices are proportional to Young's modulus times the beam width cubed. Since these terms only appeared in the stiffness matrix, the resonant frequency was directly related to their product. This implies that the analytic predictability of the resonant frequencies depended strongly on the accuracy to which both beam dimensions and Young's modulus were known. For example, for a 10% change in beam width, the predicted fundamental resonant frequency of the structure would change by about 15%. This also implies that, if the beam widths were known, the value of Young's modulus can be predicted.

EXPERIMENT

The structures were fabricated using the four-mask process developed by [3]. One of the advantages of this process was that all the critical features were defined with one mask, reducing errors due to misalignment. The structural layer defining the oscillating device was phosphorus-doped polysilicon that had been annealed at 1050°C for 30 minutes in N_2 . After the final rinse and drying, every structure was attached to the substrate, but could be freed easily with a probe tip.

The resonant frequencies, amplitudes of motion, and modes shapes of several of each of the two types of structures were determined. Structures ranging in overall length from 398 to 864 μm were tested; the curved-comb-driven structures being the shorter. All observations were made visually under 1000X magnification both

directly through a microscope and on a video monitor. Both continuous and stroboscopic illumination was used. A *dc* bias voltage was applied to *pad 1* (Figure 6) which is connected to the ground plane and semaphore structure, and to *pad 2*. The comb connected to *pad 2* needed to be set at the same potential as the semaphore structure so there would be no electrostatic attraction between the two. A sinusoidal drive voltage was applied to *pad 3*, which was connected to the other set of fixed-electrode fingers.

All testing was performed in ambient air. For all measurements of amplitude, the *dc* bias voltage was 50 V and sinusoidal driving voltage zero-to-peak amplitude was 10 V. The resonant frequencies of the semaphore structures were determined by scanning through driving voltage frequencies and finding the bands of maximum structure response amplitude. The amplitudes of the structure motion were determined by observing the difference in position between the blur envelope boundary of the resonating structure and the structure at rest.

RESULTS

A total of five multiple-mode resonant structures were tested and compared to computer simulations. Of the five, four were linear drive-base designs, and one was an angular drive-base design. Frequency predictions for all structures and all modes were generally very good. Predictions of vibration mode shapes were in moderate agreement with experiment, but occasionally, mode amplitudes were too small to determine.

Accurate simulation of the structures was dependent on knowing both the beam width and Young's modulus for the polysilicon. The fabricated beam width was measured using SEM micrographs. The dimension between the sides, the planes of which faced the same direction, of two adjacent beams gave a reference length from which other dimensions could be scaled. The beams did not have a rectangular cross-section, but an equivalent beam width, which corresponded to the actual area moment of inertia of the beam, was used in the simulation. In order to determine an estimate of Young's modulus, the value of Young's modulus used in the simulation for one single structure was varied until the predicted first resonant frequency of that structure matched the experimental first resonant frequency. The resulting estimate of the value for Young's modulus was 150 GPa; this value was the same as that found by others [2] who have used an identical fabrication process. This value for Young's modulus was used throughout the rest of the simulations.

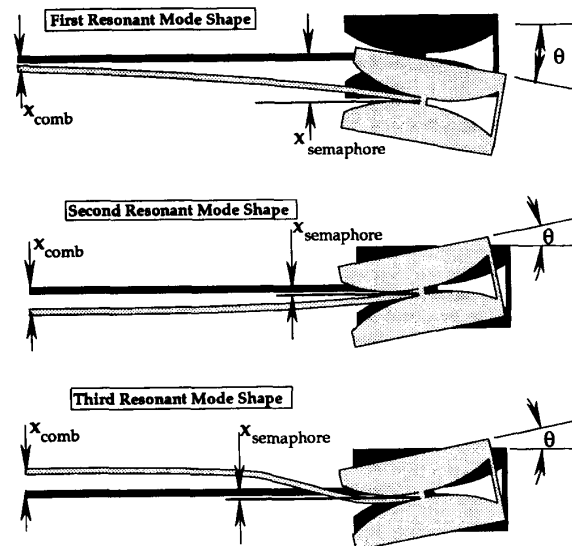


Fig. 8. First three mode shapes of the semaphore portion of a multimode resonant structure. The dark figures represent the semaphore at rest, while the light figures represent the semaphore at resonance.

Table 1. Structure dimensions

structure (drive type)	Drive-base beam length (μm)	Semaphore beam length (μm)
A (linear)	300	300 [†]
C (linear)	400	300 [†]
E (linear)	400	200 [†]
F (linear)	300	200 [†]
H (angular)	28	173 [†]

* beam tip attached to edge of semaphore mass

† beam tip attached to center of semaphore mass

Table 2. Theoretical and experimental resonant frequencies of linear and angular drive multimode resonant structures.

structure (drive type)	exp or model	Resonant Frequency (Hz)		
		1st mode	2nd mode	3rd mode
A (linear)	exp	1650 \pm 125	18,765 \pm 225	28,000 \pm 260
	model	1705	19,370	28,320
C (linear)	exp	2620 \pm 80	12,720 \pm 100	21,300 \pm 150
	model	2613	12,910	21,470
E (linear)	exp	4050 \pm 100	12,375 \pm 165	28,230 \pm 200
	model	4050	12,390	27,320
F (linear)	exp	4275 \pm 100	16,100 \pm 100	32,550 \pm 150
	model	4242	15,640	31,820
H (angular)	exp	3635 \pm 100	15,700 \pm 100	-
	model	3796	15,820	115,300

The dimensions of the five structures are shown in Table 1. Experimental and simulation results are compared in Table 2. The dynamic model predicted the mode shapes and resonant frequencies of the three perceptible resonances of the linear drive structures and of the two perceptible resonances of the angular drive structures. Once the value of Young's modulus was determined, the predicted resonant frequencies were all within 5% of the actual resonant frequencies for all mode shapes.

Three perceptible resonant frequencies and associated mode shapes were found for each of the linear drive structures and two resonant frequencies and mode shapes were found for the angular drive structures. The resonant frequencies are shown in Table 2. The mode shapes for the structures are shown in Fig. 8 and the numeric values are shown in Table 3. The mode shapes for the linear and angular drive structures were similar for the first and second modes, but no third mode was perceptible in the angular drive structures. This lack of a perceptible third mode was probably due to the shorter overall length of the angular drive structures. The short length simulation resulted in extremely high resonant frequency. A fourth resonant mode was predicted for the linear drive structures, but the lowest predicted resonant frequency for this mode was 137 kHz and resonance at this high frequency may have been precluded by the damping.

The analytic predictability of the frequency depended strongly on the accuracy of the knowledge of the beam dimensions, but simulations have shown that the mode shapes are relatively insensitive to variations in the beam width or in the value of Young's modulus. Similarly, the dynamic model showed that variations in the amount of viscous damping, assuming fully developed flow under the plate, had little effect on the predicted natural frequencies and mode shapes of the structures.

Some very long structures were fabricated. The longest structure (structure A) measured 864 μm from the free end of the semaphore mass to the attachment of the linear drive-base beams to the substrate. There was no perceptible contact between the semaphore and substrate during the testing of this device and the experimental resonant frequencies were within 3% of the predicted frequencies, implying no surface interactions or contact. A similar structure that was 964 μm long would not resonate and it is assumed that this structure did indeed contact the substrate.

Table 3. Simulated and experimental mode shapes of linear drive structure. Simulated values are normalized by the experimental value for X_2 or by X_3 if X_2 was not measurable.

structure (drive type)	resonance mode	exp or model	Zero-to-Peak Response Amplitude [†]		
			X_2 drive comb (μm)	X_3 semaphore mass (μm)	θ_3 semaphore mass (degr)
A (linear)	1st	exp	0*	1 ± 0.5	< 1
		model	0.014	1	0.2
	2nd	exp	-3 ± 1	-0*	4 ± 1
		model	-3	-0.7	2.7
C (linear)	1st	exp	0*	3 ± 1	2 ± 1.5
		model	0.2	3	0.8
	2nd	exp	-5.5 ± 1	*	6 ± 1.5
		model	-5.5	-1.6	4.6
H (angular)	1st	exp	-	4 ± 1	2 ± 1
		model	0.5	4.0	1.5
	2nd	exp	-	-1.0 ± 0.5	4 ± 1
		model	1.1	1.0	2.1

[†] negative values indicate the relative positions of the components of the structures
* not measurable

CONCLUSION

Five multiple degree-of-freedom micromechanical structures that can be tuned to respond in a desired vibration mode have been designed, fabricated, and tested. The linear and angular vibration modes of these structures can be preferentially excited. Further, the largest amplitude of structure motion can be made to occur at some distance from the drive. This can be exploited to provide the means for exciting resonant structures several hundred micrometers away from the resonating mass. Theoretical dynamic models have been developed for both the linear drive and angular drive resonant structures and these predict the resonant frequencies to within 5% as well as predict the vibrational mode shapes of the fabricated structures. The models predict no mode shape difference and little frequency change as the amount of viscous damping varies. A value of 150 GPa has been derived for Young's modulus and it matches the value reported elsewhere [2]. A resonant frequency as low as 1650 Hz has been measured for a cantilever type structure that has an overall length of 864 μm .

REFERENCES

- [1] H. Guckel, J. J. Sniogowski, T.R. Cristenson, F. Raissi, "The Application of Fine Grained, Tensile Polysilicon to Mechanically Resonant Transducers", *Transducers '89, 5th International Conference on Solid-State Sensors and Actuators*, Montreux, Switzerland, 25-30 June 1989.
- [2] William C. Tang, Tu-Cuong H. Nguyen, Michael W. Judy, and Roger T. Howe, "Electrostatic-Comb Drive of Lateral Polysilicon Resonators", *Transducers '89, 5th International Conference on Solid-State Sensors and Actuators*, Montreux, Switzerland, 25-30 June 1989.
- [3] William C. Tang, Tu-Cuong H. Nguyen, and Roger T. Howe, "Laterally Driven Polysilicon Resonant Microstructures", *IEEE Micro Electro Mechanical systems Workshop*, Salt Lake City, Utah (20-22 February 1989).
- [4] A.P. Pisano and Y.-H. Cho, "Mechanical Design Issues in Laterally-Driven Microstructures", *Transducers '89, 5th International Conference on Solid-State Sensors and Actuators*, Montreux, Switzerland, 25-30 June 1989.
- [5] Y.-C. Tai and R. S. Muller, "Frictional Study of IC-Processed Micromotors", *Transducers '89, 5th International Conference on Solid-State Sensors and Actuators*, Montreux, Switzerland, 25-30 June 1989.
- [6] K.J. Gabriel, F. Behi, R. Mahadevan, and M. Mehregany, "In Situ Friction and Wear Measurements in Integrated Polysilicon Mechanisms", *Transducers '89, 5th International Conference on Solid-State Sensors and Actuators*, Montreux, Switzerland, 25-30 June 1989.
- [7] M. Mehregany, S.F. Bart, L.S. Tavrow, J.H. Lang, S.D. Senturia, and M.F. Schlecht, "A Study of Three Microfabricate Variable-capacitance Motors", presented at *Transducers '89, 5th International Conference on Solid-State Sensors and Actuators*, Montreux, Switzerland, 25-30 June 1989.

ACKNOWLEDGEMENT

The authors would like to acknowledge the assistance, support, and efforts of Tom Booth as well as the others of the staff of the Berkeley Microfabrication Facility without whom this work would not have been successful.

APPENDIX

The stiffness matrix $[K_1]$ for the linear drive is defined as follows.

$$[K_1] =$$

$$\begin{bmatrix} 4(g_2 + g_1) & -4g_2 & 0 & 0 \\ -4g_2 & 4(g_2 + g_3) & -2g_3 & 2g_2Q_6 \\ 0 & -2g_3 & 2g_3 & -2g_3Q_6 \\ 0 & 2g_3Q_6 & -2g_3Q_6 & \frac{2g_2}{3}(l_3^2 + 3l_3b + 3b^2) \end{bmatrix}$$

where

$$g_1 = \frac{d_1}{l_1} \quad g_2 = \frac{d_2}{l_2} \quad g_3 = \frac{d_3}{l_3}$$

$$d_1 = 6 \frac{EI_1}{l_1} \quad d_2 = 6 \frac{EI_2}{l_2} \quad d_3 = 6 \frac{EI_3}{l_3}$$

$$Q_6 = \frac{l_3 + 2b}{2}$$

l_1 , l_2 , and l_3 are the area moments of inertia of the beams and l_1 , l_2 , l_3 , and b are defined in Fig. 9.

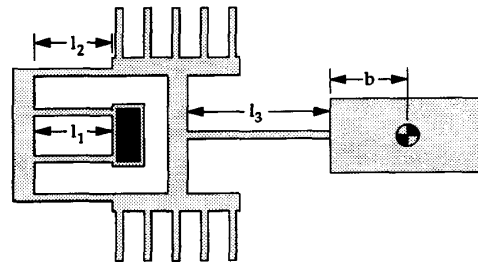


Fig. 9. Definitions for dimensions of linear drive structure.

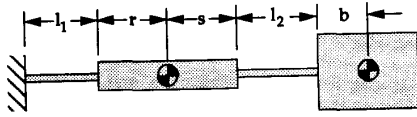


Fig. 10. Definitions for dimensions of angular drive structure.

The stiffness matrix $[K_a]$ for the angular drive is defined as follows.

$$[K_a] = \begin{bmatrix} 2(g_2 + g_1) & (Q_4 g_2 - \frac{Q_2 g_1}{3}) & (-2g_2) & (2Q_1 g_2) \\ -(\frac{Q_2 g_1}{3} + 2g_2 Q_5) & (\frac{d_1 + d_2}{6} + \frac{g_1 Q_2^2}{18} - g_2 Q_4 Q_5) & (2g_2 Q_5) & -(\frac{d_1}{6} + 2g_2 Q_1 Q_5) \\ (-2g_2) & (-g_2 Q_4) & (2g_2) & (-2Q_1 g_2) \\ (2g_2 Q_1) & (g_2 Q_1 Q_4 - \frac{d_1}{6}) & (-2g_2 Q_1) & (2g_2 Q_1^2 + \frac{d_1}{6}) \end{bmatrix}$$

where

$$g_1 = \frac{d_1}{l_1^2} \quad g_2 = \frac{d_2}{l_2^2}$$

$$d_1 = 6 \frac{E I_1}{l_1} \quad d_2 = 6 \frac{E I_2}{l_2}$$

$$Q_1 = \frac{l_2 + 2b}{2} \quad Q_2 = 3(l_1 + 2r)$$

$$Q_3 = g_2(Q_1 - (s + l_2 + b)) \quad Q_4 = l_2 + s$$

$$Q_5 = Q_1 - (s + l_2 + b)$$

I_1 and I_2 are the area moments of inertia of the beams and l_1 , l_2 , r , s , and b are defined in Fig. 10.